Phys. Status Solidi B **251,** No. 5, 958–964 (2014) / **DOI** 10.1002/pssb.201350038

physica status solidi b
www.pss-b.com
basic solid state physics

Magnetic properties and crystal structure of solid-solution $Cu_2Mn_xFe_{1-x}SnS_4$ chalcogenides with stannite-type structure

F. López-Vergara*[,1], A. Galdámez[1], V. Manríquez[1], P. Barahona[2], and O. Peña[3]

[1] Facultad de Ciencias, Departamento de Química, Universidad de Chile, Santiago, Chile
[2] Facultad de Ciencias Básicas, Universidad Católica del Maule, Talca, Chile
[3] Institut des Sciences Chimiques de Rennes, UMR 6226, Université de Rennes 1, Rennes, France

Received 17 June 2013, revised 27 November 2013, accepted 7 January 2014
Published online 3 February 2014

Keywords chalcogenides, crystal structure, magnetic properties

* Corresponding author: e-mail fer_martina@u.uchile.cl, Phone: +56 (2) 2978 7267, Fax: +56 (2) 2271 3888

New solid solutions $Cu_2Mn_xFe_{1-x}SnS_4$ were prepared by direct combination of the corresponding elements at 850 °C. The crystal structure of $Cu_2Mn_{0.4}Fe_{0.6}SnS_4$ was determined by single-crystal X-ray diffraction. This phase is described in the space group $I\bar{4}2m$ where each cation is tetrahedrally coordinated to four sulfur anions in a sphalerite-like arrangement. The XRD patterns of the solid solutions $Cu_2Mn_xFe_{1-x}SnS_4$ were fully indexed in the space group $I\bar{4}2m$ and the values of the cell parameter for all phases obey the usual linear Vegard behavior. A progressive evolution of the magnetic moment in the paramagnetic state is observed when increasing the content of manganese. The negative values of the Curie–Weiss constant, θ, indicate an antiferromagnetic (AF) behavior with AF interactions, weaker by more than one order of magnitude compared to other diluted magnetic semiconductors (DMSs) with zinc-blende or wurzite crystal structure.

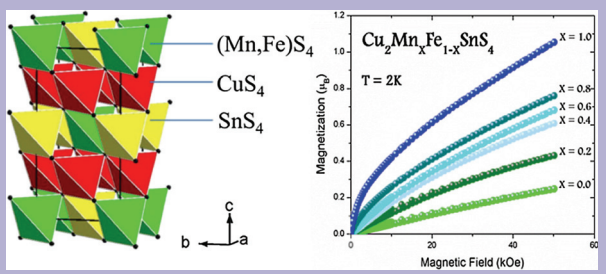

1 Introduction The diluted magnetic semiconductor (DMS) materials are of interest because of the dual character of their properties. Thus, the semiconductor nature influences the optical properties of the material, useful for information processing, while the magnetic nature allows massive storage of information. These materials have attracted renewed importance in recent years in the search to complement their properties, and booster potential applications in optoelectronics and magnetic devices [1–4]. The DMS materials that have been the most studied are alloys derived from adamantane-type structures, where each cation is coordinated to four anions and vice versa. These materials can be obtained by isomorphic substitution of a fraction of the group II cations, by paramagnetic ions such as Mn^{2+}, Fe^{2+}, Co^{2+}, etc. An example is the $Cd_{1-z}Mn_zTe$ alloy, which shows spin-glass behavior, with magneto-optical effects, bound magnetic polarons, etc. [5, 6].

In the last decades, the investigations on DMS have been focused to the important family of quaternary chalcogenides of $M_2^{1+}M^{2+}M^{4+}Q_4$ type, where M^{1+} = Cu, Ag; M^{2+} = Mn, Fe, Co, Ni, Zn, Cd; M^{4+} = Si, Ge, Sn, Pb, and Q = S, Se, Te [7–10]. The tetragonal crystal structure of these phases is based on zinc-blende or an orthorhombic superstructure for wurtzite (known as wurtz–stannite), where each cation is tetrahedrally coordinated to four sulfur anions [11–14]. In the quaternary chalcogenides takes place a reduction of symmetry, characterized by an increase in the degree of freedom in the positions of the sulfide anion, going from zinc blende (1/4, 1/4, 1/4) – chalcopyrite (x, 1/4, 1/8) – stannite (x, x, z) – kesterite (x, y, z). The phases Cu_2FeSnS_4 and

Cu_2ZnSnS_4 crystallize in the structures of stannite-type and kesterite-type, respectively [15].

The Cu_2FeSnS_4 stannite, a well-known sulfide mineral for its semiconductor properties, has been the focus of different magnetic studies, in both mineral and its synthetic materials, finding an antiferromagnetic (AF) behavior and an important magnetic anisotropy. Both, the magnetic anisotropy and exchange interactions are larger than those found in the analogous Mn-based material [8, 14]. There also has been an extensive characterization of the synthetic mineral Cu_2MnSnS_4 stannite-type, where an AF order at the Néel temperature of 20 K has been reported thanks to magnetization measurements and neutron-diffraction experiments, in addition, the neutron diffraction data showed an AF collinear structure [8].

It is known that the magnetic behavior, associated to the magnetic ions present in the structure, may modify the magnetic and optical properties of semiconductors. Thus, through the use of alloys, the properties of the DMS materials can be modulated by varying the cationic composition to achieve specific requirements. Recently, it has been suggested that quaternary chalcogenides can be good candidates for improper ferroelectricity [16].

We have previously reported the magnetic properties and crystal structures of the a new family of $Cu_2Mn_{1-x}Co_xSnS_4$ chalcogenides with kesterite type structure, where both Cu_2MnSnS_4 and Cu_2CoSnS_4 end members of the solid solutions crystallizes in the stannite space group $I\bar{4}2m$ (no. 121) [15]. In this work, we report the synthesis, structural characterization, and magnetic properties of new solid solutions $Cu_2Mn_xFe_{1-x}SnS_4$ obtained from Cu_2FeSnS_4 by replacing a fraction of the Fe^{2+} cations with the paramagnetic Mn^{2+} ion. The aim of this work is to study the influence of such substitution and of the preparation method onto the magnetic properties of the quaternary chalcogenide.

2 Experimental

2.1 Synthesis The polycrystalline new solid solutions $Cu_2Mn_xFe_{1-x}SnS_4$ and the end members Cu_2MnSnS_4 and Cu_2FeSnS_4 were prepared by direct combination of powders of the corresponding high purity elements (99.99% Aldrich). The reaction mixture was sealed in evacuated quartz ampoules, manipulated under Ar atmosphere and heated to 850 °C for about 72 h in a programmable furnace; then, the reaction mixture was cooled by quenching in liquid nitrogen. The products appeared to be air- and moisture-stable over several weeks.

2.2 Characterization Powder X-ray diffraction patterns were collected, at room temperature, on Siemens D5000 powder diffractometer, with Cu Kα radiation ($\lambda = 1.541871$ Å) in the range $5^\circ < 2\theta < 80^\circ$. The X-ray diffraction patterns were indexed with the computer program CHECKCELL.

The chemical compositions of the powder samples and single crystal were determined by scanning electron microscopy with the aid of energy-dispersive X-ray analysis (SEM-EDS) using a JEOL JXA 8600 electron microprobe (Table 1). The powder samples were compacted at $\sim 5 \times 10^8$ Pa, resulting in cylindrical pellets, mounted onto double-side carbon tape and adhered to an aluminum specimen holder. The EDS data were collected for 60 s using an accelerating voltage of 22.5 kV.

Single-crystal X-ray diffraction data of $Cu_2Mn_{0.4}Fe_{0.6}SnS_4$ were collected, at room temperature, on a Bruker Kappa CCD diffractometer, using graphite-monochromatized Mo Kα radiation ($\lambda = 0.71073$ Å). The collection of intensity data was carried out with the program COLLECT [17]. Cell refinement and data reduction were carried out with Dirax/lsq and EvalCCD programs [18, 19]. Multi-scan absorption correction was performed with SADABS program [20]. The structure was refined in full-matrix least-squares using the SHELXL crystallographic package programs [21].

Differential thermal analysis (DTA) and thermogravimetric analysis (TGA) were performed on a Simultaneous Thermal Analysis, NETZSCH STA 409. The DTA/TGA curves were run simultaneously on each sample from room temperature to 1000 °C, in flowing argon at a heating rate of 10 °C min^{-1}.

Magnetic measurements were performed on pelletized powder samples using a Quantum Design MPMS XL5 SQUID magnetometer between 2 and 400 K, under different applied fields (500 Oe for zero-field-cooled/field-cooled (ZFC/FC) cycles, and 10 kOe for measurements above T_C. Magnetization loops $M(H)$ between +50 and −50 kOe were measured at 2 K.

3 Results and discussion

3.1 Chemical and thermal analysis In order to check the purity of the investigated materials, SEM-EDS

Table 1 Chemical composition analysis (% mass) of $Cu_2Mn_xFe_{(1-x)}SnS_4$ solid solutions.

Cu	Mn	Fe	Sn	S	estimated	nominal
29.1	0	12.9	28.4	29.6	$Cu_{1.98}Fe_{1.00}Sn_{1.03}S_{3.99}$	Cu_2FeSnS_4
29.4	2.5	10.5	27.3	30.0	$Cu_{2.01}Mn_{0.20}Fe_{0.82}Sn_{1.00}S_{3.99}$	$Cu_2Mn_{0.2}Fe_{0.8}SnS_4$
29.7	4.8	8.1	27.9	29.5	$Cu_{1.99}Mn_{0.37}Fe_{0.62}Sn_{1.00}S_{3.91}$	$Cu_2Mn_{0.4}Fe_{0.6}SnS_4$
29.9	7.6	5.3	27.3	29.7	$Cu_{2.05}Mn_{0.60}Fe_{0.41}Sn_{1.00}S_{4.03}$	$Cu_2Mn_{0.6}Fe_{0.4}SnS_4$
29.3	10.5	2.4	27.8	30.0	$Cu_{1.97}Mn_{0.82}Fe_{0.18}Sn_{1.00}S_{4.00}$	$Cu_2Mn_{0.8}Fe_{0.2}SnS_4$
30.2	13.5	0	26.8	29.5	$Cu_{2.10}Mn_{1.09}Sn_{1.00}S_{4.07}$	Cu_2MnSnS_4

analyses performed in powder samples revealed that the chemical compositions were uniform throughout the scanned region and correspond fairly well to the nominal ones. The samples were found to be homogeneous within the analytical uncertainty. The chemical data are given in Table 1.

The DTA–TGA heating/cooling was conducted in argon atmosphere. The studied solid solutions behave similarly and they are stable up to aprox. 400 °C. After this temperature, they begin to decompose, a process, which occurs in two stages. The first stage of decomposition can be attributed to the partial sulfur loss. In a second stage, at 750 °C, the phases decompose totally to metal sulfides, which were identified by XRD analysis of the residues.

3.2 X-ray diffraction results In order to clarify the crystal structure of the solid solutions $Cu_2Mn_xFe_{1-x}SnS_4$, a structural study by single-crystal X-ray diffraction was performed. For this, crystals of the $Cu_2Mn_{0.4}Fe_{0.6}SnS_4$ phase were selected from the 850 °C quenched run-products. The structure was solved in the space group $I\bar{4}2m$ (N°121), which describes the structures of the compounds Cu_2MnSnS_4 and Cu_2FeSnS_4 [11, 22]. The least squares refinement converged with this model, where each cation is tetrahedrally coordinated to four sulfur anions (Fig. 1). The model with occupation sites $2a$ = (Mn, Fe) and $4d$ = Cu gave the better refinement results. Moreover, Mn and Fe atoms (same crystallographic site) were constrained to have identical thermal parameters. In addition, the refined occupation factor of Mn and Fe cations were consistent with the SEM-EDS analysis averaged over several spots of the single crystal used for the diffraction experiment.

The Fig. 1 shows the unit cell of the studied phase. This structure is based on a stannite-type arrangement of sulfur and metal atoms, in which each cation is tetrahedrally coordinated to four atoms of sulfur. Figure 2 presents a polyhedral view of the structure showing the metal layers in the ab-plane. However, unlike the stannite-type arrangements, in the phases studied herein there are cations with different valence, where the cations 2+ occupy disordered positions. Thus, in the crystal structure of $Cu_2Mn_{0.4}Fe_{0.6}SnS_4$, the (Mn, Fe) and Sn atoms share the metal layers at $z = 0$ and $z = 1/2$, and Cu atoms at $z = 1/4$ and $z = 3/4$. The metal layers are stacked parallel to the ab-plane and are separated by layers of sulfur anions.

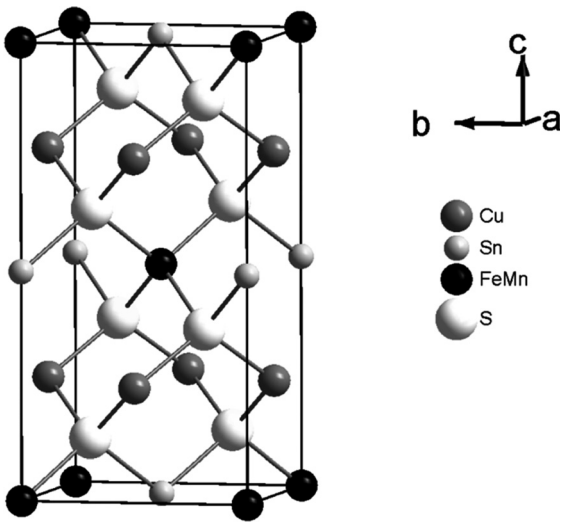

Figure 1 Unit cell of the $Cu_2Mn_{0.4}Fe_{0.6}SnS_4$ phase. The radii of the spheres are arbitrary.

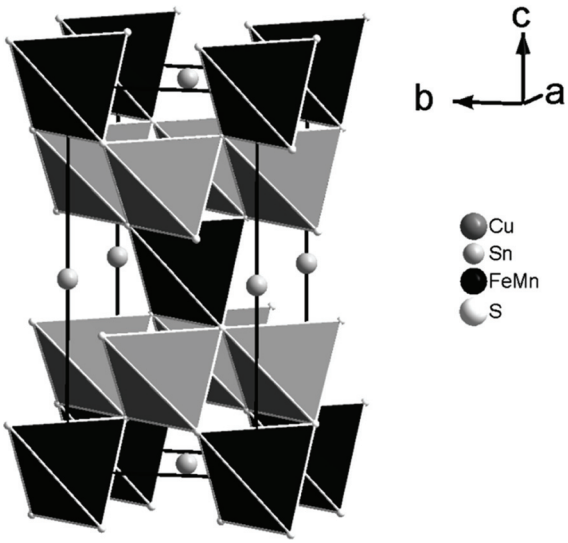

Figure 2 Polyhedral view of the crystal structure, with the tetrahedra $(Fe,Mn)S_4$ in black and tetrahedra $(Cu)S_4$ in dark gray.

Table 2 Crystallographic data and structure refinement details.

compound	$Cu_2Mn_{0.4}Fe_{0.6}SnS_4$
crystal size (mm^3)	$0.10 \times 0.07 \times 0.06$
crystal color	black
crystal system	tetragonal
space group	$I\bar{4}2m$ (N°121)
lattice constants (Å)	$a = 5.4580$ (10), $c = 10.8270$ (10)
cell volume ($Å^3$)	322.53 (9)
Z	2
density ($g\,cm^{-3}$)	4.422
temperature (K)	293(2)
wavelength (Å)	0.71073 (Mo Kα radiation)
absorption coefficient (mm^{-1})	13.551
$F(000)$	395
θ-range (°)	$4.18 < \theta < 27.49$
hkl-range	$-7 \le h \le 7$, $-7 \le k \le 7$, $-14 \le l \le 13$
no. of reflections, $R_{int.}$, R_σ	1416, 0.0998, 0.0383
no. of independent reflections	135
no. of parameters	14
extinction coefficient	0.0083 (19)
R ($I > 2\sigma_I$), R (all reflections)	0.0284, 0.0284
$wR2$ ($I > 2\sigma_I$), $wR2$ (all reflections)	0.0842, 0.0842
goodness-of-fit (GooF = S)	0.951
largest difference peaks ($eÅ^{-3}$)	1.196, −0.972

Table 3 Atomic coordinates and equivalent isotropic displacement parameters (Å^2) for $Cu_2Mn_{0.4}Fe_{0.6}SnS_4$.

atom	Wyckoff position	x	y	z	U_{eq} [a]	occ.
Cu	4*d*	½	0	¾	0.0211(6)	1.0
Fe	2*a*	0	0	1	0.0124(6)	0.60
Mn	2*a*	0	0	1	0.0124(6)	0.40
Sn	2*b*	½	½	1	0.0146(5)	1.0
S	8*i*	0.2464 (3)	0.2464 (3)	0.87055 (16)	0.0132 (7)	1.0

[a] U_{eq} is defined as one-third of the trace of the orthogonalized U_{ij} tensor.

The crystal data are summarized in Table 2. The fractional atomic coordinates and equivalent isotropic thermal parameters are listed in Table 3. The bond distances and angles are given in Table 4, and they are in agreement with the corresponding values found in stannite and kesterite structure types [11, 23]. The difference in the covalent radii of the metals causes slight distortions from the ideal tetrahedral geometry of the S sites in the MS_4 tetrahedra (M = Cu, Fe, Mn, and Sn), as observed at the bond angles S-M-S (Table 4). This has been reported for other solid solutions with kesterite and stannite structure types [11, 24, 25].

The X-ray powder diffractograms (XRD) show sharp lines that reflect the crystallinity and homogeneity. The XRD patterns of the solid solutions $Cu_2Mn_xFe_{1-x}SnS_4$ ($x = 0.2$, 0.4, 0.6, and 0.8) were fully indexed in the space group $I\bar{4}2m$ (N°121), and the observed interlayer spacing showed a good agreement with that calculated from the crystal structure. No secondary phases were observed within the limits of the experimental detection of both SEM-EDS and XRD analyses. Representative experimental diffraction profiles are shown in Figs. 3 and 4. There is significant evidence that the experimental powder pattern and calculated powder pattern from single crystal are very similar to each other. As expected, it is found a slight expansion of the cell volume due to the replacement of Fe^{2+} by Mn^{2+}, with ionic radii of 0.77 and 0.80 Å, respectively, for a tetrahedral coordination according to Shannon [26]. The values of the cell parameters for all phases are given in Table 5 and obey the Vegard's law. We propose a continuous solid solution on the basis of the cell parameter trends determined by X-ray powder diffraction.

3.3 Magnetic properties The paramagnetic regime of the solid solutions $Cu_2Mn_xFe_{1-x}SnS_4$ was measured at high fields (10 kOe), well above the magnetic transition temperature. The inverse susceptibility, $1/\chi$, was fitted by a classical Curie–Weiss relation $\chi = C/(T-\theta)$, in the range $150\,K \leq T \leq 300\,K$ (insert, Fig. 5), from which the effective moments μ_{eff} and the Curie–Weiss temperatures θ were obtained. The values of the magnetic parameters are reported in Table 6. These results show a progressive evolution of the magnetic moment in the paramagnetic state when increasing the content of manganese. In addition, the negative values of the Curie–Weiss constant, θ, indicate the existence of AF interactions.

The magnetic measurement in single-crystal of Cu_2MnSnS_4 shown $\theta = -5.2\,K$ [12] and $\theta = -32.8\,K$ in single crystal of Cu_2FeSnS_4 stannite mineral [13].

Table 4 Selected interatomic distances (Å) and angles (°) for $Cu_2Mn_{0.4}Fe_{0.6}SnS_4$.

	distances (Å)		angles (°)
M-S	2.363(2) × 4	S-M-S	110.61(5) × 4, 107.22(9) × 2
Cu-S	2.3298(10) × 4	S-Cu-S	108.29(3) × 4, 111.86(7) × 2
Sn-S	2.408(2) × 4	S-Sn-S	109.81(4) × 4, 108.79(9) × 2

M represents the 2*a* position statistically occupied by Fe (60%) and Mn (40%).

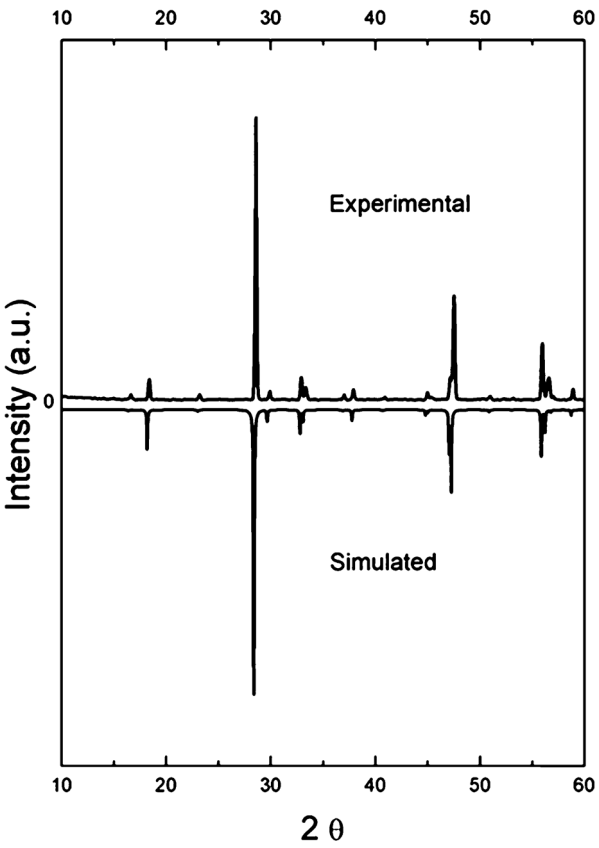

Figure 3 Experimental powder pattern $Cu_2Mn_{0.4}Fe_{0.6}SnS_4$ in comparison (like-mirror) to calculated powder pattern from single crystal of the $Cu_2Mn_{0.4}Fe_{0.6}SnS_4$.

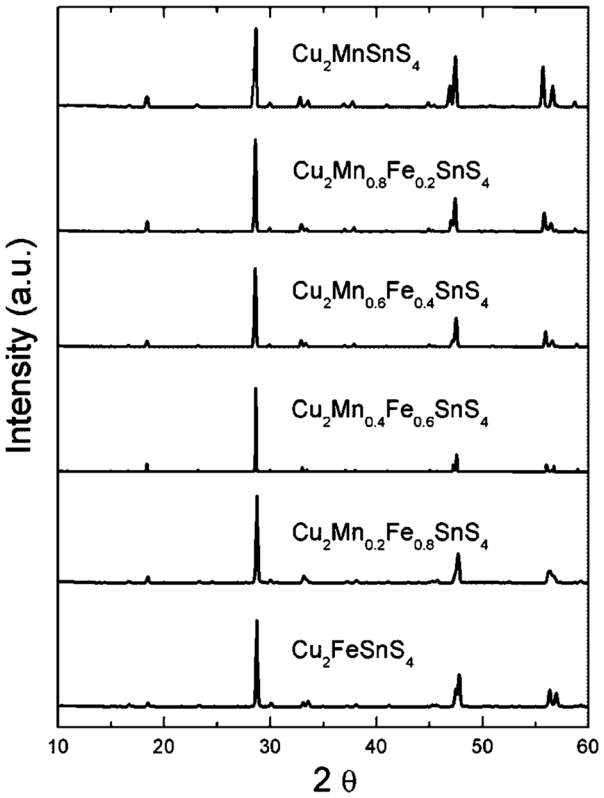

Figure 4 XRD patterns of the $Cu_2Mn_xFe_{1-x}SnS_4$ solid solutions.

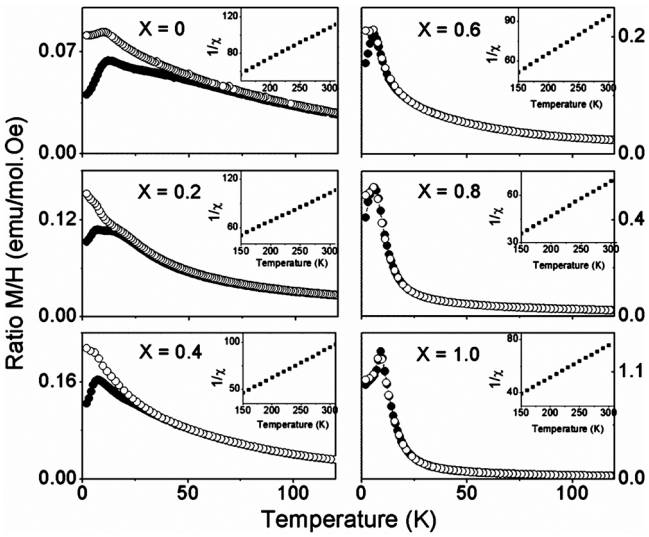

Figure 5 Zero field cooled/field cooled magnetization cycles at 100 Oe for given solid solutions (ZFC: filled symbols; FC: open symbols). The insert shows the inverse susceptibility at the paramagnetic state.

Our experimental effective moment of Cu_2FeSnS_4 ($\mu_{eff} = 4.97\,\mu_B$) is close to the expected moment for a tetrahedral high spin Fe^{2+} ($4.9\,\mu_B$) and agrees with values reported for polycrystalline samples of Cu_2FeSnS_4 ($\mu_{eff} = 5.02\,\mu_B$ [13]). The effective moment obtained at the other end-member of the solid solution Cu_2MnSnS_4 ($\mu_{eff} = 5.75\,\mu_B$), agrees with the reported values obtained in single crystal specimens ($\mu_{eff} = 5.54\,\mu_B$ [12]), although slightly lower than the theoretical moment expected for a Mn^{2+} free-spin ion ($5.92\,\mu_B$).

The ZFC/FC magnetization cycles shown in Fig. 5 were performed under low magnetic fields (500 Oe). Two different situations are observed. For samples rich in Mn ($0.6 \leq x(\mathrm{Mn}) < 1$; right-hand panels in Fig. 5) an AF transition is observed, with T_N values (Table 6) close to the one obtained by neutron diffraction experiments on Cu_2MnSnS_4 ($T_N = 20$ K [8]). When decreasing the temperature under the applied magnetic field (FC mode), a weak irreversibility is observed below T_N. For samples rich in Fe ($0 \leq x(\mathrm{Mn}) \leq 0.4$; left-hand panels in Fig. 6), the ZFC and FC magnetizations split well above the Néel temperature. This probably comes from the fact that, due to the statistical occupation of the tetrahedral site by Fe and Mn, observable contributions of two different sublattices coexist in the system, one coming from Fe nearest neighbors and another from Mn. A similar argument was advanced in the case of Cu_2FeSnS_4, in which Fe^{2+} ions occupy two antiparallel collinear sublattices below T_N [14]. It should also be noticed that the absolute values of the magnetization decrease when the x(Mn) content decreases, going from 1.2 (emu mol^{-1}) at $T = T_N$, down to 0.085 (emu mol^{-1}) when x goes from 1 to 0. To compare all samples, Fig. 6 shows the magnetization curve measured at $T = 2$ K. As it can be seen, the magnetization increases quite linearly at high fields, indicating that an AF component actually exits.

Of greater significance are the values of the Weiss constant θ. As it is known, the Weiss constant is an indirect measurement of the strength of the AF interaction and is related to the exchange constant J in a mean-field

Table 5 Lattice parameter for solid solutions $Cu_2Mn_xFe_{1-x}SnS_4$.

phase	a (Å)	c (Å)	V (Å^3)
Cu_2FeSnS_4	5.434 ± 0.004	10.734 ± 0.001	316.904 ± 0.053
$Cu_2Mn_{0.2}Fe_{0.8}SnS_4$	5.442 ± 0.010	10.753 ± 0.008	318.402 ± 0.194
$Cu_2Mn_{0.4}Fe_{0.6}SnS_4$	5.466 ± 0.005	10.767 ± 0.001	321.658 ± 0.065
$Cu_2Mn_{0.6}Fe_{0.4}SnS_4$	5.469 ± 0.003	10.791 ± 0.001	322.759 ± 0.043
$Cu_2Mn_{0.8}Fe_{0.2}SnS_4$	5.482 ± 0.012	10.789 ± 0.002	324.244 ± 0.154
Cu_2MnSnS_4	5.509 ± 0.002	10.796 ± 0.001	327.654 ± 0.033

Table 6 Magnetic data for the solid solutions $Cu_2Mn_xFe_{1-x}SnS_4$.

phase	μ_{theo} (μ_B)	μ_{eff} (μ_B)	θ (K)	T_N (K)
Cu_2FeSnS_4	4.90	4.97	−25	16
$Cu_2Mn_{0.2}Fe_{0.8}SnS_4$	5.11	5.16	−9	11
$Cu_2Mn_{0.4}Fe_{0.6}SnS_4$	5.31	5.26	−8	12
$Cu_2Mn_{0.6}Fe_{0.4}SnS_4$	5.52	5.25	−7	9
$Cu_2Mn_{0.8}Fe_{0.2}SnS_4$	5.75	5.44	−9	10
Cu_2MnSnS_4	5.92	5.75	−8	11

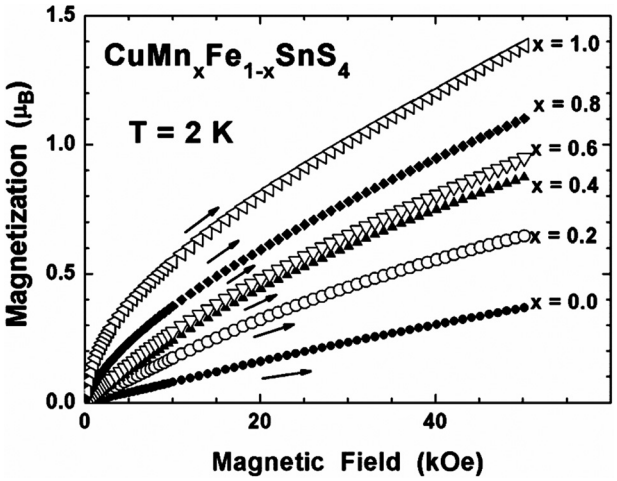

Figure 6 Magnetization curves measured at $T = 2$ K with increasing fields, for the solid solutions $Cu_2Mn_xFe_{1-x}SnS_4$.

approximation as [27]:

$$\theta = \frac{2S(S+1)}{3k}\sum m_i J_i,$$

where m_i and J_i are the number and exchange interaction for the ith set, respectively, and the summation is done over sets of equidistant magnetic neighbors from a chosen magnetic atom.

The θ values given in Table 6 indicate that the AF interactions have been reduced by more than 1 order of magnitude relative to comparable DMSs with zinc-blende or wurzite crystal structures: the β-MnS with zinc-blende structure has a $\theta = -982$ K and with wurzite structure $\theta = -932$ K [28].

For the here studied solid solutions $Cu_2Mn_xFe_{1-x}SnS_4$, where the magnetic cations Fe^{2+} and Mn^{2+} form a body-centered tetragonal lattices, it is possible to propose three exchange constants J_i, in a similar manner to Cu_2MnSnS_4 with stannite structure, in which Fe^{2+} or Mn^{2+} ions are separated by lattice constants a, $a\sqrt{3/2}$, and $a\sqrt{2}$, respectively [8]. Then, the magnetic interactions between cations occur at distances of approximately 5.5 Å, compared to the approximately 3.8 Å in sphalerite and wurzite. Thus, the main reason why the AF exchange interactions are weaker in the studied phases may be due that there are fewer neighbors, within a given sublattice, connected by J_i exchange bonds and some of them are frustrated because of the disorder of the cations in the sublattice.

4 Conclusions We have investigated the effects of the partial substitution of the Fe^{2+} cations by the paramagnetic ion Mn^{2+} on the structural and magnetic properties of Cu_2(Mn, Fe)SnS_4 phases. We found that the synthesized solid solutions $Cu_2Mn_xFe_{1-x}SnS_4$ are homogeneous and they all index in the space group $I\bar{4}2m$ (N°121). The variation of the lattice volume is in agreement with the ionic radius of the substituting element. The crystal structure of the phase $Cu_2Mn_{0.4}Fe_{0.6}SnS_4$, determined by single-crystal X-ray diffraction, shows a stannite structure type described in the space group $I\bar{4}2m$ (N°121). The chemical replacement of Fe^{2+} by Mn^{2+} is accompanied by a partial substitution in the stannite-type structure: Mn replaces partially Fe at the sites 2*a* (0,0,0). For its part, the Cu atoms are ordered at 4*d* (0, ½, ¼ and ½, 0, ¼). The studied solid solutions shows AF behavior with AF interactions reduced by more than 1 order of magnitude compared to other DMSs with zinc-blende or wurzite crystal structure. A progressive evolution of the magnetic moment in the paramagnetic state is observed when increasing the content of manganese.

Acknowledgements Research financed by grant FONDECYT N° 1110161 and ECOS-CONICYT C09 E01. Authors are members of France-Chile Joint International Laboratory LIA-MIF CNRS N°836. The authors thank to Vincent Dorcet (CDIFX of the Université de Rennes 1, France) for the X-ray intensity data collections.

References

[1] H. Ohno, Science **281**, 951–956 (1998).
[2] T. Dietl, H. Ohno, F. Matsukura, J. Cibert, and D. Ferrand, Science **287**, 1019–1022 (2000).
[3] T. Dietl, Semicond. Sci. Technol. **17**, 377–392 (2002).
[4] E. Quintero, M. Quintero, E. Moreno, L. Lara, M. Morocoima, F. Pineda, P. Grima, R. Tovar, P. Bocaranda, J. A. Henao, and M. A. Macías, J. Phys. Chem. Solids **71**, 993–998 (2010).
[5] Y. Shapira, E.J. McNiff, Jr., N.F. Oliveira, Jr., E. D. Honing, K. Dwight, and A. Wold, Phys. Rev. B **37**, 411 (1988).
[6] U. Verma, S. Sharma, N. Devi, P. Bisht, and P. Rajaram, J. Magn. Magn. Mater. **323**, 394 (2011).
[7] X. L. Chen, A. M. Lamarche, G. Lamarche, and J. C. Woolley, J. Magn. Magn. Mater. **118**, 119–128 (1993).
[8] T. Fries, Y. Shapira, F. Palacio, M. C. Moro, G. J. Mcintyre, R. Kershaw, A. Wold, and E. J. McNiff, Jr., Phys. Rev. B **56**, 5424–5431 (1997).
[9] G. H. Mccabe, T. Fries, M. T. Liu, Y. Shapira, R. Kershaw, A. Wold, C. Fau, M. Averous, and E. J. Mcniff, Phys. Rev. B **56**, 6673–6680 (1997).
[10] E. Quintero, M. Quintero, E. Moreno, M. Morocoima, P. Grima, P. Bocaranda, J. A. Henao, and J. Pinilla, J. Alloys Compd. **471**, 16–20 (2009).
[11] S. R. Hall, J. T. Szymansk, and J. M. Stewart, Can. Miner. **16**, 131–137 (1978).

[12] L. Guen and W. S. Glaunsinger, J. Solid State Chem. **21**, 10–21 (1980).
[13] G. P. Bernardini, D. Borrini, A. Caneschi, F. Di Benedetto, D. Gatteschi, S. Ristori, and M. Romanelli, Phys. Chem. Miner. **27**, 453–461 (2000).
[14] A. Caneschi, C. Cipriani, F. Di Benedetto, and R. Sessoli, Phys. Chem. Miner. **31**, 190–193 (2004).
[15] F. López-Vergara, A. Galdámez, V. Manríquez, P. Barahona, and O. Peña, J. Solid State Chem. **198**, 386–391 (2013).
[16] G. Nénert and T. T. M. Palstra, J. Phys.: Condens. Matter **21**, 176002 (2009).
[17] COLLECT, Software for CCD diffractometers, Bruker AXS, Inc., Madison, WI (1997–2004).
[18] A. J. M. Duisenberg, R. W. W. Hooft, A. M. M. Schreurs, and J. Kroon, J. Appl. Crystallogr. **33**, 893 (2000).
[19] A. J. M. Duisenberg and A. M. M. Schreurs, J. Appl. Crystallogr. **36**, 220 (2003).
[20] SADABS, Area-Detector Absorption Correction, Siemens Industrial Automation, Inc., Madison, WI (1996).
[21] G. SHELXL-97, Program for solution and refinement of crystal structures, Sheldrick GM, University of Göttingen (1997).
[22] P. Bonazzi, L. Bindi, G. P. Bernardini, and S. Menchetti, Can. Miner. **41**, 639–647 (2003).
[23] L. Brockway and Z. Kristallogr, **89**, 434 (1934).
[24] T. Bernert and A. Pfitzner, Z. Kristallogr. **220**, 968–972 (2005).
[25] T. Bernert and A. Pfitzner, Z. Anorg. Allg. Chem. **632**, 1213–1218 (2006).
[26] R. D. Shannon, Acta Crystallogr. A **32**, 751–767 (1976).
[27] J. S. Smart, Effective Field Theory of Magnetism (W.B. Saunders, Philadelphia, 1966).
[28] L. Corliss, N. Elliott, and J. Hastings, Phys. Rev. **104**, 924–928 (1956).

